Hybrid Quantum Dot–Fatty Ester Stealth Nanoparticles: Toward Clinically Relevant *in Vivo* Optical Imaging of Deep Tissue

Adam J. Shuhendler,[†] Preethy Prasad,[†] Ho-Ka Carol Chan,[†] Claudia R. Gordijo,[†] Behrouz Soroushian,[‡] Michael Kolios,[‡] Kui Yu,[§] Peter J. O'Brien,[†] Andrew Michael Rauth,[⊥,*] and Xiao Yu Wu[†,*]

[†]Leslie L. Dan Faculty of Pharmacy, University of Toronto, 144 College Street, Toronto, Ontario, Canada, M5S 3M2, [‡]Department of Physics, Ryerson University, 350 Victoria Street, Toronto, Ontario, Canada, M5B 2K3, [§]NRC Steacie Institute for Molecular Sciences, National Research Council of Canada, 100 Sussex Drive, Ottawa, Ontario, Canada, K1A 0R6, and [⊥]Department of Medical Biophysics, University Health Network, Princess Margaret Hospital, 610 University Avenue, Toronto, Ontario, Canada, M5G 2M9

ABSTRACT Despite broad applications of quantum dots (QDs) *in vitro*, severe toxicity and dominant liver uptake have limited their clinical application. QDs that excite and emit in the ultraviolet and visible regions have limited *in vivo* applicability due to significant optical interference exerted by biological fluids and tissues. Hence we devised a new biocompatible hybrid fluorophore composed of near-infrared-emitting PbSe quantum dots encapsulated in solid fatty ester nanoparticles (QD-FEN) for *in vivo* imaging. The quantum yield and tissue penetration depth of the QD-FEN were characterized, and their biological fate was examined in a breast tumor-bearing animal model. It was found for the first time that chemical modification of the headgroup of QD-encapsulating organic fatty acids was a must as these groups quenched the photoluminescence of PbSe nanocrystals. The use of fatty esters enhanced aqueous quantum yields of PbSe QDs up to ~45%, which was 50% higher than that of water-soluble PbSe nanocrystals in an aqueous medium. As a result, a greater than previously reported tissue penetration depth of fluorescence was recorded at 710 nm/840 nm excitation/emission wavelengths. The QD-FEN had much lower short-term cytotoxicity compared to nonencapsulated water-soluble QDs. More importantly, reduced liver uptake, increased tumor retention, lack of toxic response, and nearly complete clearance of QD-FEN from the tested animals was demonstrated. With a combination of near-infrared spectral properties, enhanced optical properties,and significantly improved biosafety profile, this novel hybrid nanoparticulate fluorophore system demonstrably provides real-time, deep-tissue fluorescent imaging of live animals, laying a foundation for further development toward clinical application.

KEYWORDS: hybrid quantum dot–fatty ester nanoparticles · high biocompatibility · deep tissue penetration · near-infrared whole-body imaging · breast tumor model

Medical imaging has become a staple in a clinician's arsenal for the detection and treatment of human disease, especially for cancers.[1] Current imaging modalities applied to oncology, such as magnetic resonance imaging and positron emission tomography (PET), require expensive instrumentation and long subject exposure times. In the case of PET, potentially genotoxic radioisotope contrast agents are employed.[2] In contrast, fluorescent imaging methods utilizing nonionizing radiation are relatively less expensive and less hazardous, and can be performed quickly with brief exposure times. However, traditional fluorescent imaging in medicine has been severely limited by light scattering and autofluorescence of tissue in the ultraviolet and visible light range.[3,4] Hence images have only been acquired at depths of a few millimeters below the surface of the skin.[3,4] In the near-infrared (NIR) wavelength range of 650–900 nm, the light scattering, absorbance, and autofluorescene of tissue are at a minimum, providing an opportunity for deeper optical interrogations *in vivo* with a predicted tissue penetration depth of 1–2 cm (Figure 1).[4,5] Whether or not fluorescent medical imaging can become of broad use in clinical practice now depends on the development of a safe, biocompatible fluorophore with excitation and emission wavelengths in the NIR.

Ideally, an NIR fluorophore for medical applications should have a large absorption exctinction coefficient, high NIR quantum yield, low photobleaching, and no toxicity.[6] Organic fluorophores are poor candidates for deep fluorescent medical imaging because of their poor circulation half-lives, poor NIR quantum yields, rapid photobleaching, and spectral shifting due to rapid plasma protein binding, metabolism, and/or chemical degradation.[6–8] For this reason, NIR-tuned semiconductor quantum dots (QD) have been developed and applied to medical imaging for sentinal lymph node mapping[9–11] and tumor imaging.[12,13] The properties of QDs that render them effective fluorophores for medical fluorescence imaging

*Address correspondence to xywu@phm.utoronto.ca.

Received for review November 8, 2010 and accepted December 27, 2010.

Published online February 21, 2011
10.1021/nn103024b

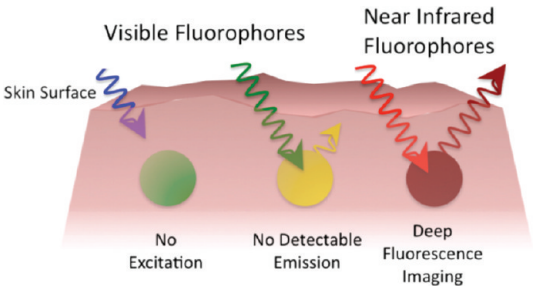

Figure 1. Schematic representation of the utility of fluorophores in the visible (green, yellow) *versus* the near-infrared (dark red) for deep fluorescence imaging. In the visible region, due to light scattering and absorption by living tissue, poor penetration of the excitation photon into the skin (green) or the penetration of the emission photon out of the skin (yellow) prevents the detection of the fluorophore signal *in vivo*. Photons in the near-infrared are capable of deep tissue penetration.

stem from their high quantum yields with NIR excitation and their large effective Stoke's shifts, resulting in the potential for optical image acquisition at greater tissue depths.[3,14,15] Currently, however, the major hurdle in the clinical application of QDs as medical-grade fluorophores is their toxicity,[16] attributable to the heavy metal precursors required for their synthesis,[17] the ligands employed for their surface functionalization,[18] and their extensive liver uptake and poor clearance rates that result in unsafe pharmacokinetic profiles.[19,20] By mitigating the toxicity issues of QDs through improvement of their pharmacokinetic profiles while maintaining their superior spectral properties in the NIR region, an inorganic QD-organic fatty ester nanoparticle hybrid fluorophore has been formulated. These particles may be well suited for medical imaging applications, advancing the field of fluorescence medical imaging.

RESULTS AND DISCUSSION

This paper describes the formulation and characterization of quantum dots encapsulated in fatty ester nanoparticles. The novel nanocarrier system can effectively encapsulate NIR PbSe QDs resulting in lower *in vitro* cytotoxicity, improved *in vivo* biodistribution, and clearance of the semiconductor nanocrystals, and enhanced aqueous QD optical properties resulting in deep-tissue imaging capabilities. While QDs emitting in the visible range have previously been encapsulated in lipid-based nanoparticles,[21] this paper presents the first encapsulation of QDs with clinically relevant optical properties in stealth, fatty ester-based nanoparticles, the first demonstration of improved aqueous quantum yield of QDs, and a vast improvement of imaging depth, resulting in significant progress toward enhanced fluorophore biocompatibility and utility.

Formulation of QD-FEN. Lead−selenide (PbSe) nanocrystals were employed for the formulation of QD-FENs due to their relative ease of synthesis, the tunability of their emisson within the NIR range, their high resultant quantum yields with NIR excitation, and the demonstrated photostability of this semiconductor system.[14,15,22] The synthesis of PbSe QDs was based on a room temperature scheme under ambient atmospheric conditions previously published, resulting in hydrophobic, oleic acid-capped nanocrystals, ~7 nm in diameter that were suspended in hexanes.[15] The formulated QD-loaded fatty acid or fatty ester nanoparticles were 110 ± 15 nm in hydrodynamic diameter, as measured by dynamic light scattering, with the PbSe QD being trapped within the now solid matrix (Figure 2A). The measured zeta potential ($\zeta = -20 \pm 1.3$ mV) was favorable to both a stable emulsion and to good biocompatibility. The Myrj block copolymers used in the formulation are essential to both stabilize the molten nanoemulsion droplets and coat the surface of the solidified nanoparticles with poly(ethylene glycol) chains, imparting enhanced biocompatilibity to the QD-FENs (Figure 2A). The coating of nanoparticles with a poly(ethylene glycol) corona has previously been shown to impart a stealth property to liposomal formulations, evading the recognition and uptake by the reticuloendothelial system thus extending the circulation time of the particles in the body.[23] Under electron microscopic imaging, the PbSe QDs were clearly seen as black spots within the matrix of the QD-FENs (Figure 2B). The electron density characteristic of metal particles was absent in electron micrographs of QD-free fatty ester nanoparticles (Figure 2C).

Spectral Characteristics of QD-FEN. The PbSe QDs in our hands showed an emission maximum at 860 nm (Figure 3A) and a quantum yield in hexanes of ~15% at an excitation wavelength (λ_{ex}) of 710 nm, as determined using 1,1′-diethyl-4,4′-carbocyanine iodide as the quantum yield standard (λ_{ex} = 710 nm, λ_{em} = 735 nm, quantum yield =3.6%[24]). Suprisingly, when PbSe QDs were encapsulated in myristic acid-based nanoparticles, near complete quenching of the QD emission was observed (Figure 3A). Initially, this novel QD quenching phenomenon was attributed to either the physical transition of the QD environment from a liquid to a solid phase as the nanoemulsion was cooled and the fatty droplets were solidified, or to the presence of the carboxylic acid headgroups of the fatty acid chains. To investigate each potential cause separately, PbSe QDs were synthesized and suspended in *n*-octanol or 1-octanoic acid, and the fluorescence emission spectra were recorded (Figure 3B). Since both dispersing media were liquid at room temperature, any fluorescence quenching would only be due to the presence of the carboxylate of the octanoic acid and not the physical phase of the medium itself. The photoluminescence curves obtained provided strong evidence that the fluorescence quenching of the QDs by the myristic acid nanoparticles was due to the carboxylate groups of the fatty acid matrix. To mask the carboxylate groups of the fatty acid matrix, fatty acid ethyl esters of eicosanoic acid

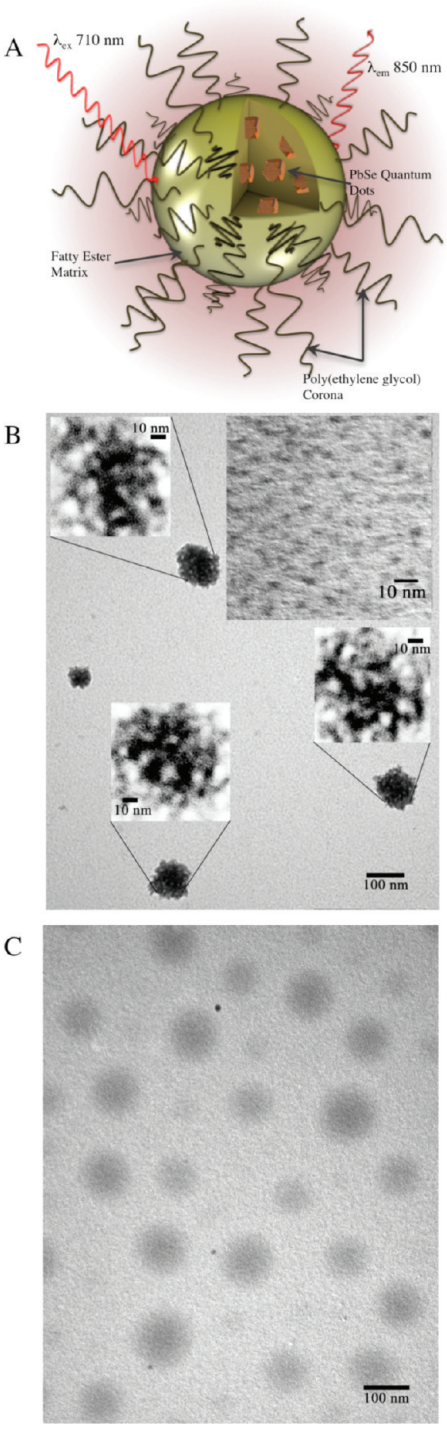

Figure 2. PbSe QDs are dispersed throughout the matrix of QD-FENs, which bear a corona of poly(ethylene glycol), as shown in the schematic A. Transmission electron micrographs of QD-FENs (B) and fatty ester nanoparticles (C) clearly demonstrate the encapsulation of the metal QDs within the fatty matrix. Transmission electron micrograph of PbSe QDs on their own is shown in the top right inset of panel B. Scale bars in panels B and C are 100 nm, scales bars in insets of panel B are 10 nm.

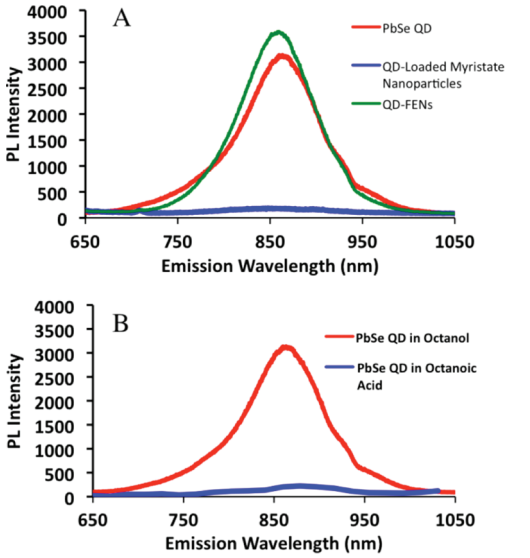

Figure 3. (A) The photoluminescence quenching of PbSe QDs encapsulated in solid fatty acid nanoparticles is clear by comparing the emission spectra of free PbSe QDs (red) to the emission of QD-loaded myristate nanoparticles (blue), as is the reversal of this quenching effect with QD-FENs (green). (B) The appearance of this quenching effect when QDs were dispersed in 1-octanoic acid (blue) but not in *n*-octanol (red) suggests that the hydrophobic fatty acid moiety of the fatty carrier matrix as the cause of the QD signal attenuation.

were synthesized according to previously published methods[25] and QD-FENs were formulated. The return of the strong photoluminescence at 860 nm was observed (Figure 3A), providing further evidence that the previously observed QD fluorescence quenching was due to the interaction of the carboxylate groups of the fatty acid with the surface of the PbSe QDs and not due to the liquid-to-solid phase transition of the nanoparticulate carrier matrix.

Unexpectedly with the use of ethyl eicosanoate as the carrier matrix, the quantum yield of QD-FENs suspended in water increased 3-fold over free PbSe QDs suspended in hexanes, from ~15% to ~45%, determined at λ_{ex} = 710 nm with 1,1′-diethyl-4,4′-carbocyanine iodide as the quantum yield standard. The previously published quantum yield for water-soluble PbSe QDs stabilized by (1-mercaptoundec-11-yl)tetra(ethylene glycol) (MTPEG) was 30%,[15] making our QD-FEN formulation 50% more efficient, spectrally, than the free water-soluble QDs. The enhanced fluorescence efficiency of QD-FENs can be ascribed to the protection of QDs in a hydrophobic nanoenvironment of fatty ester matrix. The preparation of water-soluble QDs involves exchange of hydrophobic ligand with hydrophilic ones and direct dispersion of QDs in aqueous medium, which have previously been shown to decrease the quantum yield of PbSe QDs.[15] In our formulation the PbSe QDs are maintained in their oleic acid cap and encapsulated in the hydrophobic matrix of QD-FENs. Thus they are never in direct contact with the aqueous medium, leading to high quantum yields.

Imaging Depth of Penetration of QD-FEN. One limitation of medical fluorescence imaging is the shallow distance of image acquisition, often to below 10 mm from the surface of the skin.[6] To quantitatively measure the

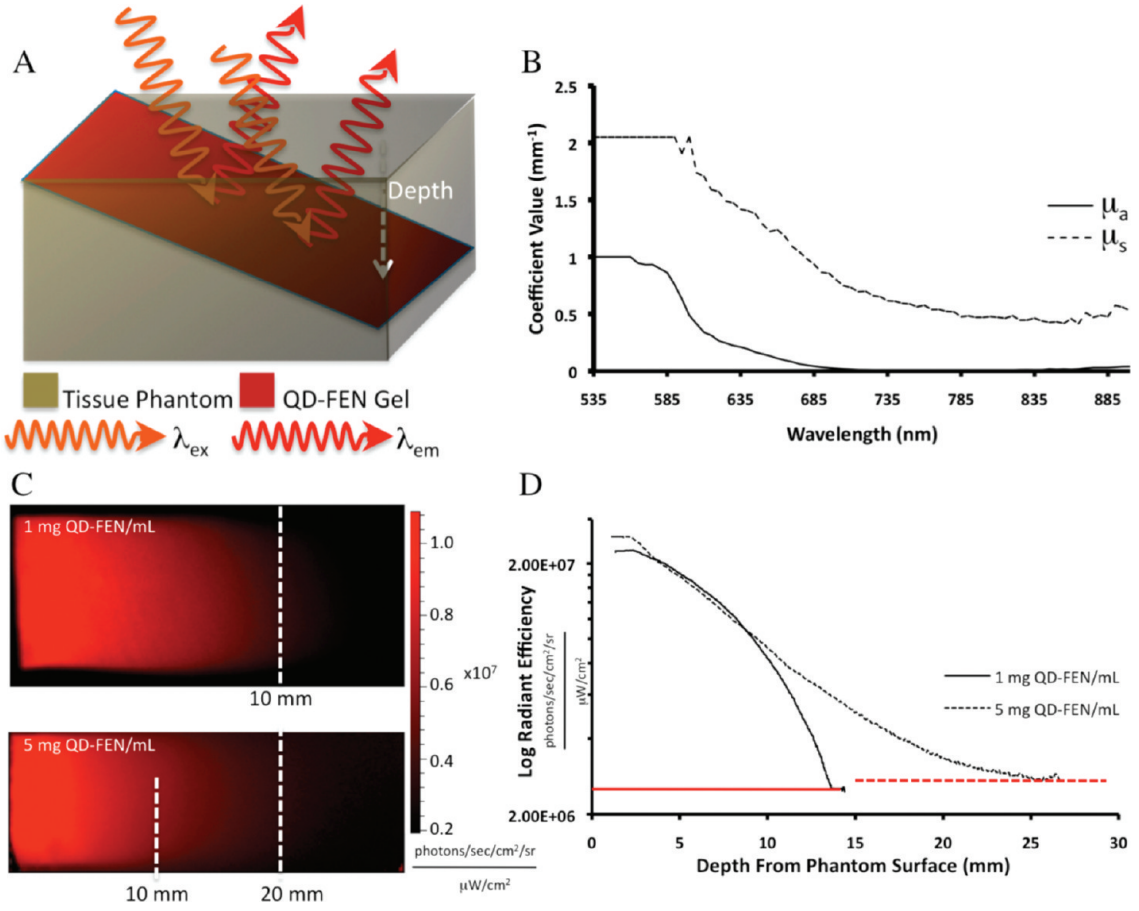

Figure 4. Quantitative, continuous measurement of fluorophore signal tissue depth penetration in a tissue phantom model. (A) Schematic diagram of the tissue phantom constructed for depth penetration measurements, showing the 1-mm thick gel (red) containing QD-FENs encased at an angle within the tissue-like phantom (brown). The depth measurements account for excitation photon (λ_{ex}, orange) and emission photon (λ_{em}, red) penetration. (B) The light scattering and light absorption characteristics of the tissue phantom characterized by the scattering (μ_s, dotted) and absorption (μ_a, solid) coefficients, respectively, as measured by two integrating spheres in series. (C) Fluorescent images taken from the top of a 1.5 cm (1 mg QD-FEN/mL, top) and 2.7 cm (5 mg QD-FEN/mL, bottom) maximal QD-FEN gel depth phantom, illustrating disappearance of detectable signal as a function of gel depth. (D) A plot of the pixel intensity *versus* tissue phantom depth of the phantoms depicted in Figure 4C, quantifying the maximal penetration of the 1 mg QD-FEN/mL gel to ~1.3 cm (solid) and of the 5 mg QD-FEN/mL gel to ~2.4 cm (dotted). Backgound fluorescence levels are indicated by a solid red line for the 1 mg QD-FEN/mL phantom and a dotted red line for the 5 mg QD-FEN/mL phantom.

depth of image acquisition possible using QD-FENs, a novel system for the continuous measurement of biologically relevant imaging depth was developed and implemented (Figure 4). Gelatin tissue phantoms were created, mimicking the absorbance and scattering characterisitcs of living tissue as previously reported.[26] Gelatin, hemoglobin, sodium azide, and Intralipid were mixed at elevated temperatures and were poured into a prechilled plastic mold tilted at an ~45° angle (Figure 4A). A 1-mm thick gelatin slab was cast containing the desired dilution of QD-FENs, and was laid on top of the bottom portion of the set gelatin−hemoglobin−Intralipid phantom. The mold containing the diagonal phantom bottom and the encapsulated QD slab was set flat on a surface and was slowly filled with more gelatin−hemoglobin−Intralipid mixture heated to 40 °C. The addition of warm phantom mixture slightly melted the hardened phantom, preventing the formation of a phantom−phantom interface to yield a single solid phantom mass (Figure 4A). Measures of the distance a photon could travel in the phantom before the photon was absorbed (μ_a) or scattered (μ_s) were performed on 1-mm thick samples of the tissue phantom using two integrating spheres in series to prevent cross talk between absorption and scattering measurements (Figure 4B), and were found to be in agreement with the same parameters of real tissue.[26] The 1-mm thick slab containing the QD-FENs continuously and nearly linearly decreased in depth from one side of the phantom to the other, permitting the quantification of fluorescence signal strength as a function of phantom depth from a single fluorescent image acquired with a Xenogen IVIS Spectrum whole animal imager (Figure 4C). Quantification of the signal intensity *versus* depth was performed with ImageJ,[27] yielding the plot of signal intensity *versus* penetration depth in Figure 4D. From this plot, it can be seen that the QD-FENs showed strong signal penetration beyond 20

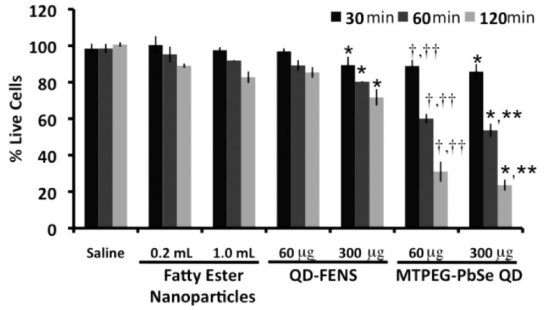

Figure 5. The toxicity of QD-FENs or PbSe QDs in their free, water-soluble form was assessed *in vitro* in a rat hepatocyte assay for accelerated assessment of cytotoxicity. Saline, fatty ester nanoparticles, QD-FENS, and water-soluble QDs (MTPEG-PbSe QD) were incubated at a low (60 μg) and high (300 μg) dose in 10 mL of cell suspension, and cytotoxicity was assessed at 30 min (black), 60 min (dark gray), and 120 min (light gray). Statistical comparisons of survival data of QD-FEN and MTPEG-PbSe QD against fatty ester nanoparticles for each dosing level were performed using a Nested ANOVA and *posthoc* Tukey's Test. (†) Significant differences ($p < 0.05$) in survival rates between low dose fatty ester nanoparticles, and QD-FEN or MTPEG-PbSe QD. (††) Significant differences ($p < 0.05$) in survival rates between low dose QD-FEN and MTPEG-PbSe QD. (∗) Significant differences ($p < 0.05$) in survival rates between high dose fatty ester nanoparticles and QD-FEN or MTPEG-PbSe QD. (∗∗) Significant differences ($p < 0.05$) in survival rates between high dose QD-FEN and MTPEG-PbSe QD. Data represent the mean and standard deviation of three trials.

mm, reaching nearly 25 mm in depth with 5 mg QD-FENs/mL phantom containing a total of 1.6 mg of PbSe QDs. Previous quantitative investigations of the penetration depth of fluorescence of NIR fluorophores have reported limits up to 9.7 mm,[26] less than half of the penetration depth of the QD-FENs. By increasing the quantum yield of the encapsulated QDs, it is reasonable to postulate that this depth of penetration may be significantly extended.

Toxicity Assessment of QD-FEN. The main limitation preventing the application of semiconductor nanocrystals to medical fluorescent imaging is the toxicity arising from their heavy metal constituents,[17] their surface capping and functionalizing agents,[18] and their poor pharmacokinetic performance,[19] for example, accumulating mainly in the liver without being cleared.[20] In the case of PbSe QDs, the well-known toxicity of Pb[28] and the potential toxicity of Se at high doses[29] limit the biomedical applications of this nanocrystal in its free form. As a preliminary assessment of the safety of QD-FEN for *in vivo* use, the toxicity of QD-FENs was assessed against water-soluble MTPEG-capped PbSe QDs using isolated rat hepatocytes. This model has been used for rapid toxicity screening and has demonstrated *in vitro*−*in vivo* toxicity extrapolation.[30] Water-soluble, MTPEG−PbSe QDs showed significant hepatocyte toxicity, resulting in less than 40% hepatocyte survival upon exposure to 6 μg/mL of PbSe QDs after 120 min (Figure 5). Exposure of hepatocytes to the same dose of PbSe QDs in QD-FENs for 120 min resulted in the survival of 80% of hepatocytes. Even after exposure to 30 μg/mL of QD-FENs for 120 min, approximately 70% of hepatocytes still survived. The fatty ester nanoparticle itself has been shown to be biocompatible *in vitro*[31] and *in vivo*,[32] a result that was confirmed with the hepatocyte toxicity screening assay presented herein. The reduced toxicity of QD-FENs may arise from the mitigation of two processes involved in QD toxicity: the loss of free heavy metal ions from QD degradation[17] and the aggregation of the QDs in tissue due to loss of the water-soluble capping ligand from the nanocrystal surface.[6,18] The degradation of the nanocrystal into its free metal ions is thought to occur in the endolysosomal compartment of the cells following QD uptake, a compartment that is acidic and promotes metal ion loss. Since PbSe QDs are trapped within the solid matrix core of the fatty ester carrier (Figure 2), the endolysosomal acidification is unlikely to reach the fatty ester encased QDs, resulting in maintenance of structural integrity and prevention of free Pb^{2+} leaching. Since the PbSe QDs in their hydrophobic, oleic acid capped state favorably interact with the hydrophobic core of the fatty ester nanoparticles that are stabilized by PEG and surfactant, their aggregation becomes moot. As a result, the encapsulation of PbSe QDs in the unique hydrophobic, biocompatible matrix of fatty ester nanoparticles significantly reduces the toxicity of PbSe QDs *in vitro*. The low acute toxicity of QD-FEN observed in this preliminary test is encouraging suggesting the enhanced biocompatibility of PbSe QDs. However further assessment of *in vivo* end points of PbSe QD toxicity in more detail is required to establish the safety profile of QD-FEN.

***In Vivo* Whole Animal Imaging With QD-FEN.** To both demonstrate the utility of QD-FENs for deep tissue, whole animal fluorescent imaging, and preliminarily assess the *in vivo* fate and tolerability of this formulation, 200 μL of QD-FENs in saline suspension (64 μg of PbSe QD total) was injected intravenously in the tail vein of nude mice (Figure 6A). The mice were inoculated in the inguinal mammary fat pad with a human breast tumor cell line (MDA435) stably expressing green fluorescent protein. The subiliac lymph node was used as a landmark for tumor inoculation in the mammary fat pad. The tumor can be seen in the leftmost panel of Figure 6A after 3 weeks of growth using whole animal fluorescent imaging. At this point the QD-FENs were injected intravenously. Mice were imaged intact for 7 days to determine both the distribution of the fluorescent hybrid nanoparticle, as well as the clearance of the fluorophore over time. Background fluorescence can be seen in the "background" panel of Figure 6A, with mostly intestinal background due to porphyrins in the mouse chow. Following the intravenous injection of QD-FENs, clear, bright fluorescence can be seen. Within the first 2 h of administration, broad fluorescence was observed throughout the animal with bright spots in the abdominal region.

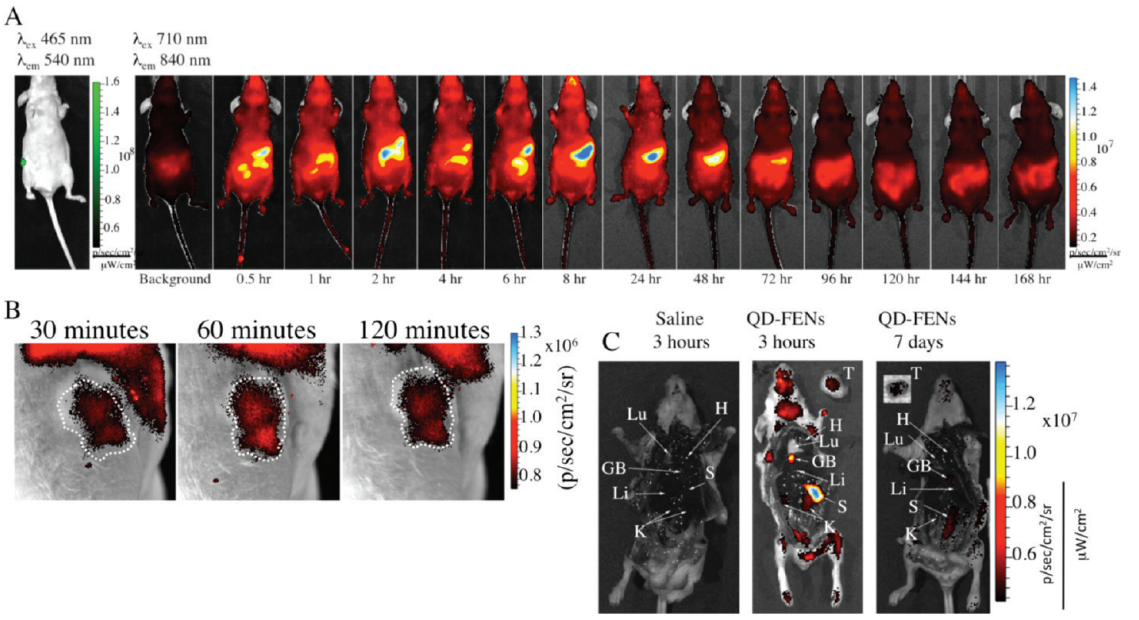

Figure 6. The formulation of QD-FENs provides for deep, real-time, *in vivo* fluorescence imaging following intravenous administration, providing favorable biodistribution and clearance of the nanocrystal cargo. (A) The biodistribution of QD-FENs in a green fluorescent protein-expressing MDA435 model of human breast cancer was followed over 7 days with whole animal fluorescent imaging: (right) fluorescent image of the breast tumor; (left) longitudinal biodistribution and elimination of the QD-FENs. (B) Tumor accumulation of the QD-FENs was noted by 30 min after intravenous administration. (C) Necropsy analysis of the tissue distribution showed significant accumulation of QD-FENs in the spleen and gall bladder, without accumulation in the liver after 3 h. Near complete elimination of the QD-FENs was observed 7 days after administration: GB, gall bladder; H, heart, K, kidney; Li, liver; Lu, lung; S, spleen; T, tumor.

Suprisingly, none of the abdominal fluorescence arose from the liver, which is the main site of uptake of free, water-soluble QDs and the main site of QD retention that results in the poor biocompatibility of the fluorophore.[20] From 4 to 8 h after injection, the QD-FENs were seen to accumulate in the spleen, and this accumulation could be seen to decrease to nearly preinjection levels by 96 h after injection. Within 7 days (168 h), the whole animal fluorescence decreased to nearly background levels, providing preliminary evidence that the encapsulation of PbSe QDs in fatty ester nanoparticles can enhance the biocompatibility of QDs by enabling near complete clearance of the fluorophore from the body. This is in contrast to the application of free QDs *in vivo*, as long-term retention and poor clearance have been noted to be the major cause of concern regarding the application of semiconductor nanocrystals in a clinical setting.[19,20,33] By zooming in on the mammary fat pad area of the animal, tumor fluorescence above tissue background could be noted by 1 h (60 min) after QD-FEN injection, indicating the passive accumulation of QD-FENs within the tumor tissue (Figure 6B). A post-mortem examination of nude mice 3 h after injection with saline, 3 h after QD-FEN injection, and 7 days following QD-FEN injection revealed accumulation of the QD-FENs primarily in the spleen and gall bladder at 3 h, with some accumulation in the kidneys (Figure 6C). The renal accumulation decreased to background and the QD-FENs were almost completely cleared from the spleen and gall bladder by 7 days. No hepatic, heart, or lung accumulation was noted even at 3 h after injection, further demonstrating that the danger of hepatic uptake of the PbSe QDs was mitigated by encapsulation in the solid fatty ester nanoparticles. Of note is confirmation of the passive accumulation of the QD-FENs in the tumor by 3 h after injection and the retention of some of the QD-FENs even at 7 days after administration. This preliminary assessment of the novel nanocomposite QD-FEN demonstrates the synergy of enhanced biocompatibility through optimized tissue distribution and clearance with enhanced aqueous optical efficiency, resulting in an advancement in the applicability of QDs to deep tissue, macroscopic, fluorescent imaging. A shortcoming of nontomographic fluorescence imaging employed in this work is the inability to distinguish the precise depth profile of the QD-FEN *in vivo*. To precisely locate the QD-FEN in three-dimensional space in an animal, further studies are in progress using fluorescence molecular tomography. In addition, an in depth assessment of the retention of Pb^{2+} in body tissues and longer term tissue toxicity following intravenous administration of QD-FENs will need to follow. The results of this study will have a large impact on the possible application of NIR QDs to medical fluorescent imaging applications.

CONCLUSIONS

Noninvasive, nonionizing, and low cost deep fluorescent imaging can provide rapid, high spatial and temporal resolution images and may present a new

frontier in medical imaging modalities. While the work presented here uses single photon excitation for whole animal fluorescence imaging, innovation in multiphoton imaging instrumentation continues to advance the possible applicability of this modality. Similar innovative strides need to be made in the development of biocompatible NIR fluorophores for deep tissue imaging so that, in combination with instrumentation innovation, fluorescent medical imaging may become a reality. Here we present the formulation of a novel nanocomposite fluorophore of PbSe QDs encapsulated in a stealth fatty ester nanoparticle carrier. Along with demonstrated enhanced spectral efficiency and deeper tissue imaging capability, this system boasts an improved safety profile that contributes to the mitigation of concerns regarding the *in vivo* use of water-soluble semiconductor nanocrystals. While the liver-sparing biodistribution and more complete elimination results are preliminary, work is in progress to quantify these important characteristics of this NIR nanocomposite fluorophore.

METHODS

Myristic acid, eicosanoic acid, poly(ethylene oxide)-40-stearate (Myrj 52), poly(ethylene glycol)-100-stearate (Myrj 56), lead oxide, selenium, trioctylphosphine, oleic acid, octadecene, hexanes, 1,1′-diethyl-4,4′-carbocyanine iodide, methanol, ethanol, chloroform, octanoic acid, octanol, (1-mercaptoundec-11-yl)tetra(ethylene glycol), hemoglobin, Intralipid, Trizma base, sodium chloride, cupric acetate, butanol, and acetyl chloride were purchased from Sigma-Aldrich and used without further purification. Gelatin was purchased from J. T. Baker, and sodium azide was purchased from Fisher Scientific. Pluronic F-68 was purchased from BASF. Type II Collagenase was purchased from Worthington. $CDCl_3$ was purchased from CIL. Human breast cancer MDA435 cells were purchased from ATCC. Nude mice (NCR-NU-F) were purchased from Taconic, Inc.

Synthesis of Fatty Esters. Fatty esters were synthesized as previously reported.[25] Briefly, eicosanoic acid was dissolved in chloroform, to which an ethanolic solution of cupric acetate, as well as ethanolic HCl, was added. This solution was stirred for 1 h, after which time the reaction was quenched with distilled deionized water, and the fatty ester was extracted with chloroform. The chloroform was evaporated under nitrogen gas, yielding a white solid. The solid was dissolved in $CDCl_3$, and the structure was confirmed by standard ^1H NMR and ^{13}C NMR performed on a Varian Mercury 300 MHz instrument. The proton and carbon NMR spectra of the fatty ester and the fatty acid are given in the Supporting Information. No residual eicosanoic acid can be seen in either NMR spectrum, indicating its complete conversion to ester.

Synthesis of PbSe Quantum Dots. PbSe quantum dots were synthesized according to previously published methods.[15] Briefly, lead oxide was dissolved in octadecene and oleic acid under a nitrogen atmosphere at 150 °C. Once dissolved, the solution was cooled, opened to ambient air, and a solution of selenium in trioctylphosphine was added. This solution was stirred for 4 h, after which time the quantum dots were isolated through the addition of butanol and methanol. For preparation of water-soluble QD for toxicity assessment, the exchange of oleic acid for MTPEG on the PbSe QD surface was accomplished as previously described.[15] The fluorescence spectra of the PbSe QDs were recorded on an Ocean Optics spectrofluorimeter.

Formulation of QD-FENs. The fatty esters prepared in this work, Myrj 52, and Myrj 56, were heated to 80 °C until melted. The molten mixture was stirred and PbSe QD suspended in hexanes was added. The mixture was stirred for 20 min to allow for the evaporation of hexanes and dispersion of the QDs in the molten fatty ester. An aqueous solution of Pluronic F68 was then added to the molten mixture, followed by distilled deionized water preheated to 80 °C. This emulsion was ultrasonicated using a Hielscher UP-100S probe sonicator (100 W, 30 kHz) for 5 min. Immediately following sonication, the entire emulsion was dispersed in cold 0.9% saline. Particle size and zeta potential were measured on a Nicomp 380 Zetasizer by dynamic light scattering and electrophoretic light scattering, respectively. Particle morphology and QD loading were assessed by transmission electron microscopy of unstained samples using a Hitachi H-7000 microscope.

Preparation of Tissue Phantom. Tissue phantoms were prepared based on the compositions reported previously.[26] Tris-buffered saline was poured on top of a known amount of sodium azide and gelatin to make a final concentration of 15 mM and 10w/v% respectively. The mixture was heated to 50 °C using a water bath (Haake D8 Immersion heater) with constant stirring by a Caframo BDC 1850 overhead stirrer at 650−800 rpm. After the gelatin had dissolved, the mixture was cooled to 37 °C with constant stirring. Hemoglobin and intralipid were added to reach concentrations of 170 μM and 1 v/v%, respectively.

A gel cassette intended for electrophoresis was used as a mold to form a 1 mm thick slab of tissue phantom containing QD-FEN. QD-FEN in saline was mixed with a warm phantom mixture at 1 mg of QD-FE/mL or 5 mg of QD-FEN/mL concentrations. For the 5 mg QD-FEN/mL slab, extra gelatin was added to make a final gelatin solution of 10 wt % in order to ensure proper slab solidification. All glassware used was warmed to 37 °C to prevent premature solidification of the phantom mixture. The warm QD-FEN mixture was then pipetted into the space between the two glass plates almost to the brim. The entire set up was then placed in refrigeration (4 °C) until it solidified.

The construction of the tissue phantom is outlined in Supporting Information, Figure S2. Before phantom construction, the mold was kept under refrigeration to ensure rapid solidification of the phantom and prevent intralipid separation. To construct the bottom layer of the phantom, the mold was tilted such that the bottom was inclined to 45°. Warm tissue phantom mixture was poured to a desired depth and tapped to remove any air bubbles. The bottom layer was refrigerated until solid. The remainder of the tissue phantom mixture was kept warm at 37 °C with constant stirring. The QD-FEN slab was removed from the electrophoresis gel cassette and trimmed to fit the mold. The slab was then laid midline across the length of the bottom tissue phantom layer, and any air bubbles were smoothed out. Warm tissue phantom mixture was poured over top to fill the mold, and the mold was refrigerated until solidified. For depths approximately 3 cm or deeper, warm tissue phantom was poured and solidified layer-by-layer to prevent dissolution of the QD-FEN slab layer. Solidified tissue phantom was removed from the mold by running a thin spatula around the edge. Once complete, the tissue phantom was stored at 4 °C until needed. Excess tissue phantom mixture or QD-FEN slab mixtures were also stored at 4 °C, to be melted at 37 °C for reuse.

Optical Characterization of Tissue Phantom. To ensure that the composition of the tissue phantom produced a gel with optical properties comparable to that of human tissue, the scattering coefficient (μ_s) and absorption coefficient (μ_a) were quantified using integrating spheres. The sample was mounted between 2 BK7, 1 mm thick optical windows (Esco Products), which were separated by a 1 mm thick spacer. The spacer had a cutout at the top so that the phantom mixture could be poured in before it solidified. A halogen white light source (HL-2000, Ocean Optics) was used, *via* focusing lenses, to illuminate the sample when it

was mounted in a reflectance−transmittance (RT) integrating sphere system. The 6 in. diameter integrating spheres (SphereOptic) were mounted one at a time to eliminate cross talk. The R sphere was mounted in front of the sample position and reflectance, background, and reference signal spectra were recorded. The R sphere was then removed and the T sphere was mounted behind the sample. The transmittance, background, and reference spectra were recorded. A Monte Carlo simulation using 10^6 photons and an asymmetry parameter = 0.9 generated a lookup table which matched the R and T values with μ_a and μ_s values.

Tissue Phantom Image Acquisition and Data Analysis. Tissue phantoms were imaged using a Xenogen IVIS Spectrum instrument in epifluorescence mode. The phantom was placed on the stage and images were taken with automatic exposure and aperture settings in field of view C. One image was taken from the top of the gel phantom, and a second image was taken of the cross section of the gel. Intensity scales were set to a monochromatic (red) type with units of radiant efficiency and the range was set to full.

ImageJ[27] was used for image analysis, which comprised four steps:

(1) Using the monochromatic scale, a calibration of pixel intensity versus the intensity value in radiant efficiency was performed. The dimensions of the intensity scale were determined in pixels, allowing the dimensions of one pixel to be determined in terms of the intensity scale dimensions. ImageJ was then used to determine the pixel-by-pixel intensity of the intensity scale bar, allowing for a plot of pixel intensity versus radiant efficiency to be generated.

(2) Using the top view image of the gel phantom, the pixel intensity versus the distance in millimeters from the origin (selected to be the topmost point of the QD-FEN slab in the gel phantom) was determined. The determination of the dimensions of a pixel allowed for a plot of pixel intensity versus distance in millimeters from the origin to be generated.

(3) Using the cross-sectional image, the depth of the QD-FEN gel slab was determined from the top of the gel phantom, resulting in a plot of distance from the origin versus QD-FEN slab depth.

(4) Combining the plot of pixel intensity versus distance from the origin (Step 2) with the plot of distance from the origin versus QD-FEN slab depth (Step 3), a plot of pixel intensity in radiant efficiency versus QD-FEN slab depth was generated, as shown in Figure 4D.

Determination of Cytotoxicity of QDs and QD-FENs. Hepatocytes were isolated from rats by perfusion of the liver with collagenase as described previously.[34] Isolated hepatocytes (10^6 cells/mL) (10 mL) were suspended in Krebs−Henseleit buffer (pH 7.4) containing 12.5 mM HEPES in continually rotating 50 mL round-bottomed flasks, under an atmosphere of 95% O_2 and 5% CO_2 in a water bath of 37 °C for 30 min. Hepatocyte viability was assessed microscopically by plasma membrane disruption as determined by the trypan blue (0.1% w/v) exclusion test.[35] Hepatocyte viability was determined at 30, 60, and 120 min, and the cells were at least 80−90% viable before use.

Transfection of Tumor Cell. Human MDA435 breast adenocarcinoma cells were stably transfected to express enhanced green fluorescent protein (EGFP). The EGFP plasmid (pEGFP-N1, Clonetech) was linearized by digestion with the restriction endonuclease Dra III (New England Biolabs), and was transfected into the cells by incubation with $CaPO_4$. After 24 h of incubation, cells were grown in selection media containing minimal essential medium supplemented with 10% fetal calf serum and 600 μg/mL of the selection antibiotic G418. Cell colonies that formed and that were fluorescent were lifted and plated in selection medium in individual wells of a 24-well microplate. The three best colony expansions, determined by fluorescent intensity and number of fluorescent cells, were selected for sorting by fluorescence activated cell sorting (FACS). The brightest 20% of each of the three expanded colonies were selected by FACS and were further expanded in regular growth medium.

***In Vivo* Whole Animal Imaging in Tumor-Bearing Mice.** To establish orthotopic xenograft breast tumors, 1 million human MDA435 cells expressing EGFP were injected into the inguinal mammary fat pads of nude mice using the subiliac lymph node as an injection landmark. This ensured greater mouse-to-mouse reproducibility of the tumor model. Tumors were monitored for growth with fluorescent imaging during the course of the three-week growth period. Mice were injected with QD-FEN formulation into the lateral tail veins and anaesthetized with isoflurane. Images were acquired using a Xenogen IVIS Spectrum whole animal imager with λ_{ex} = 710 nm and λ_{em} = 840 nm. All animal work was approved by the animal care committee at the University Health Network, and all experiments were performed in accordance with all guidelines and regulations put forth by the Canadian Council on Animal Care.

Acknowledgment. The authors gratefully thank the Canadian Breast Cancer Foundation-Ontario Region for funding the work herein, the National Science and Engineering Council of Canada, the University of Toronto and the Ben Cohen Fund for providing scholarships to A. Shuhendler. The authors also acknowledge A. Worthington for performing the measurements of the optical properties of the tissue phantoms, J. T. Henderson for providing the enhanced green fluorescent protein plasmid used to label the tumor cells, M. Monroy for technical assistance with the mammary fat pad mouse model, and STTARR for technical assistance with fluorescence imaging.

Supporting Information Available: Further experimental details regarding the NMR characterization of fatty acid ester structure and the construction of the tissue phantom for quantification of optical probe fluorescent depth penetration. This material is available free of charge *via* the Internet at http://pubs.acs.org.

REFERENCES AND NOTES

1. Holm, B. A.; Bergey, E. J.; De, T.; Rodman, D. J.; Kapoor, R.; Levy, L.; Friend, C. S.; Prasad, P. N. Nanotechnology in Biomedical Applications. *Mol. Cryst. Liq. Cryst. Sci. Technol., Sect. A* **2002,** *374*, 589.
2. Aswathy, R. G.; Yoshida, Y.; Maekawa, T.; Kumar, D. S. Near-Infrared Quantum Dots for Deep Tissue Imaging. *Anal. Bioanal. Chem.* **2010,** *397*, 1417.
3. Altinoglu, E. I.; Adair, J. H. Near Infrared Imaging With Nanoparticles. *Wiley Interdiscip. Rev. Nanomed. Nanobiotechnol.* **2010,** *2*, 461.
4. Smith, A. M.; Mancini, M. C.; Nie, S. Bioimaging: Second Window for *in Vivo* Imaging. *Nat. Nanotechnol.* **2009,** *4*, 710.
5. Ntziachristos, V.; Bremer, C.; Weissleder, R. Fluorescence Imaging With Near-Infrared Light: New Technological Advances That Enable *in Vivo* Molecular Imaging. *Eur. Radiol.* **2003,** *13*, 195.
6. Ghoroghchian, P. P.; Therien, M. J.; Hammer, D. A. *In Vivo* Fluorescence Imaging: A Personal Perspective. *Wiley Interdiscip. Rev. Nanomed. Nanobiotechnol.* **2009,** *1*, 156.
7. Prasad, P. N. *Introduction to Biophotonics*; John Wiley and Sons: Hoboken, NJ, 2003.
8. Santra, S.; Dutta, D. Nanoparticles for Optical Imaging of Cancer. In *Nanomaterials for Cancer Diagnosis*; Challa, S. S. R. K., Ed.; Wiley-VCH Verlag GmbH: Weinheim, Germany, 2007; 44.
9. Ballou, B.; Ernst, L. A.; Andreko, S.; Harper, T.; Fitzpatrick, J. A.; Waggoner, A. S.; Bruchez, M. P. Sentinel Lymph Node Imaging Using Quantum Dots In Mouse Tumor Models. *Bioconjugate Chem.* **2007,** *18*, 389.
10. Kim, S.; Lim, Y. T.; Soltesz, E. G.; De Grand, A. M.; Lee, J.; Nakayama, A.; Parker, J. A.; Mihaljevic, T.; Laurence, R. G.; Dor, D. M.; *et al.* Near-Infrared Fluorescent Type II Quantum Dots for Sentinel Lymph Node Mapping. *Nat. Biotechnol.* **2004,** *22*, 93.
11. Zimmer, J. P.; Kim, S. W.; Ohnishi, S.; Tanaka, E.; Frangioni, J. V.; Bawendi, M. G. Size Series of Small Indium Arsenide−Zinc Selenide Core−Shell Nanocrystals and Their Application to *In Vivo* Imaging. *J. Am. Chem. Soc.* **2006,** *128*, 2526.

12. Cai, W.; Shin, D. W.; Chen, K.; Gheysens, O.; Cao, Q.; Wang, S. X.; Gambhir, S. S.; Chen, X. Peptide-Labeled Near-Infrared Quantum Dots for Imaging Tumor Vasculature in Living Subjects. *Nano Lett.* **2006,** *6*, 669.
13. Diagaradjane, P.; Orenstein-Cardona, J. M.; Colon-Casasnovas, N. E.; Deorukhkar, A.; Shentu, S.; Kuno, N.; Schwartz, D. L.; Gelovani, J. G.; Krishnan, S. Imaging Epidermal Growth Factor Receptor Expression *In Vivo*: Pharmacokinetic and Biodistribution Characterization of a Bioconjugated Quantum Dot Nanoprobe. *Clin. Cancer Res.* **2008,** *14*, 731.
14. Du, H.; Chen, C.; Krishnan, R.; Krauss, T. D.; Harbold, J. M.; Wise, F. W.; Thomas, M. G.; Silcox, J. Optical Properties of Colloidal PbSe Nanocrystals. *Nano Lett.* **2002,** *2*, 1321.
15. Evans, C. M.; Guo, L.; Peterson, J. J.; Maccagnano-Zacher, S.; Krauss, T. D. Ultrabright PbSe Magic-Sized Clusters. *Nano Lett.* **2008,** *8*, 2896.
16. Azzazy, H. M.; Mansour, M. M.; Kazmierczak, S. C. From Diagnostics to Therapy: Prospects of Quantum Dots. *Clin. Biochem.* **2007,** *40*, 917.
17. Cho, S. J.; Maysinger, D.; Jain, M.; Roder, B.; Hackbarth, S.; Winnik, F. M. Long-Term Exposure to CdTe Quantum Dots Causes Functional Impairments in Live Cells. *Langmuir* **2007,** *23*, 1974.
18. Hardman, R. A Toxicologic Review of Quantum Dots: Toxicity Depends on Physicochemical and Environmental Factors. *Environ. Health Perspect.* **2006,** *114*, 165.
19. Bentolila, L. A.; Ebenstein, Y.; Weiss, S. Quantum Dots for *in Vivo* Small-Animal Imaging. *J. Nucl. Med.* **2009,** *50*, 493.
20. Yang, R. S.; Chang, L. W.; Wu, J. P.; Tsai, M. H.; Wang, H. J.; Kuo, Y. C.; Yeh, T. K.; Yang, C. S.; Lin, P. Persistent Tissue Kinetics and Redistribution of Nanoparticles, Quantum Dot 705, in Mice: ICP−MS Quantitative Assessment. *Environ. Health Perspect.* **2007,** *115*, 1339.
21. Liu, W.; He, Z.; Liang, J.; Zhu, Y.; Xu, H.; Yang, X. Preparation and Characterization of Novel Fluorescent Nanocomposite Particles: CdSe/ZnS Core−Shell Quantum Dots Loaded Solid Lipid Nanoparticles. *J. Biomed. Mater. Res. A* **2008,** *84*, 1018.
22. Ouyang J.; Schuurmans C.; Zhang Y.; Nagelkerke R.; Wu X.; Kingston D.; Wang Z. Y.; Wilkinson D.; Li C.; Leek M. D.; *et al.* Low-Temperature Approach to High-Yield and Reproducible Syntheses of High-Quality Small-Sized PbSe Colloidal Nanocrystals for Photovoltaic Applications. *ACS Appl. Mater. Interfaces* 2010, DOI: am-2010−01129m.R1,
23. Gabizon, A. A. Stealth Liposomes and Tumor Targeting: One Step Further in the Quest for the Magic Bullet. *Clin. Cancer Res.* **2001,** *7*, 223.
24. Benson, R. C.; Kues, H. A. Absorption and Fluorescence Propertes of Cyanine Dyes. *J. Chem. Eng. Data* **1977,** *22*, 379.
25. Hoshi, M.; Williams, M.; Kishimoto, Y. Esterification of Fatty Acids at Room Temperature by Chloroform−Methanolic HCl−Cupric Acetate. *J. Lipid Res.* **1973,** *14*, 599.
26. De Grand, A. M.; Lomnes, S. J.; Lee, D. S.; Pietrzykowski, M.; Ohnishi, S.; Morgan, T. G.; Gogbashian, A.; Laurence, R. G.; Frangioni, J. V. Tissue-like Phantoms for Near-Infrared Fluorescence Imaging System Assessment and the Training of Surgeons. *J. Biomed. Opt.* **2006,** *11*, 014007.
27. Abramoff, M. D.; Magelheas, P. L.; Ram, S. J. Image Processing with ImageJ. *Biophoton. Int.* **2004,** *11*, 36.
28. Patocka, J.; Cerny, K. Inorganic Lead Toxicology. *Acta Med. (Hradec Kralove)* **2003,** *46*, 65.
29. MacFarquhar, J. K.; Broussard, D. L.; Melstrom, P.; Hutchinson, R.; Wolkin, A.; Martin, C.; Burk, R. F.; Dunn, J. R.; Green, A. L.; Hammond, R.; *et al.* Acute Selenium Toxicity Associated with a Dietary Supplement. *Arch. Intern. Med.* **2010,** *170*, 256.
30. O'Brien, P. J.; Chan, K.; Silber, P. M. Human and Animal Hepatocytes *in Vitro* with Extrapolation *in Vivo*. *Chem. Biol. Interact.* **2004,** *150*, 97.
31. Shuhendler, A. J.; Cheung, R. Y.; Manias, J.; Connor, A.; Rauth, A. M.; Wu, X. Y. A Novel Doxorubicin−Mitomycin C Co-encapsulated Nanoparticle Formulation Exhibits Anticancer Synergy in Multidrug Resistant Human Breast Cancer Cells. *Breast Cancer Res. Treat.* **2010,** *119*, 255.
32. Wong, H. L.; Rauth, A. M.; Bendayan, R.; Wu, X. Y. *In Vivo* Evaluation of a New Polymer−Lipid Hybrid Nanoparticle (PLN) Formulation of Doxorubicin in a Murine Solid Tumor Model. *Eur. J. Pharm. Biopharm.* **2007,** *65*, 300.
33. Mansur, H. S. Quantum Dots and Nanocomposites. *Wiley Interdiscip. Rev. Nanomed. Nanobiotechnol.* **2010,** *2*, 113.
34. Moldeus, P.; Hogberg, J.; Orrenius, S. Isolation and Use of Liver Cells. *Methods Enzymol.* **1978,** *52*, 60.
35. Moridani, M. Y.; Pourahmad, J.; Bui, H.; Siraki, A.; O'Brien, P. J. Dietary Flavonoid Iron Complexes as Cytoprotective Superoxide Radical Scavengers. *Free Radical Biol. Med.* **2003,** *34*, 243.